Development of a handheld integrating sphere snow grain sizer (HISSGraS)

Teruo Aoki[1] (iD), Akihiro Hachikubo[2] (iD), Motoshi Nishimura[1] (iD), Masahiro Hori[3] (iD), Masashi Niwano[4] (iD), Tomonori Tanikawa[4] (iD), Konosuke Sugiura[3] (iD), Ryo Inoue[5] (iD), Satoru Yamaguchi[6] (iD), Sumito Matoba[7] (iD), Rigen Shimada[8] (iD), Hiroshi Ishimoto[4] (iD) and Jean-Charles Gallet[9] (iD)

[1]Arctic Observation Center, National Institute of Polar Research, Tachikawa, Japan; [2]Environmental and Energy Resources Research Center, Kitami Institute of Technology, Kitami, Japan; [3]School of Sustainable Design, University of Toyama, Toyama, Japan; [4]Meteorological Research Institute, Japan Meteorological Agency, Tsukuba, Japan; [5]The Graduate University for Advanced Studies, SOKENDAI, Tachikawa, Japan; [6]Snow and Ice Research Center, National Research Institute for Earth Science and Disaster Resilience, Nagaoka, Japan; [7]Institute of Low Temperature Science, Hokkaido University, Sapporo, Japan; [8]Earth Observation Research Center, Japan Aerospace Exploration Agency, Tsukuba, Japan and [9]Norwegian Polar Institute, Tromsø, Norway

Abstract

We developed a Handheld Integrating Sphere Snow Grain Sizer (HISSGraS) for field use to measure the specific surface area (SSA) of snow. In addition to snow samples, HISSGraS can directly measure snow surfaces and snow pit walls. The basic measurement principle is the same as that of the IceCube SSA instrument. The retrieval algorithm for SSA from reflectance employs two conversion equations formulated using spherical and nonspherical grain shape models. We observed SSAs using HISSGraS, IceCube and the gas adsorption method in a snowfield in Hokkaido, Japan. Intercomparison of the results confirmed that with HISSGraS direct measurement, SSA profile observations can be completed in just ~1/10 the time required for measurement of snow samples. Our results also suggest that HISSGraS and IceCube have similar accuracy when the same snow samples are measured using the same grain shape model. However, SSAs of near-surface snow layers measured using the three techniques exhibited some biases, possibly due to rapid snow metamorphism or melting during measurement and some technical issues with optical techniques. When excluding SSA data for the surface layer, which metamorphosed remarkably during measurement, IceCube- and HISSGraS-derived SSAs correlated strongly with those obtained by gas adsorption and HISSGraS accuracy is 21–34%.

1. Introduction

Snow grain size and the specific surface area (SSA, the ratio of surface area to mass or volume) of snow grains are important physical parameters for characterizing the evolution of snow metamorphism (Schneebeli and Sokratov, 2004; Dominé and others, 2007) and are responsible for the snow surface albedo (Wiscombe and Warren, 1980; Aoki and others, 2003, 2011). The spectral albedo of snow at near-infrared (NIR) wavelengths depends strongly on snow grain size, while in the visible the main contribution is due to snow impurities (Warren and Wiscombe, 1980; Wiscombe and Warren, 1980). Thus, the surface albedo over clean (i.e. low-impurity) snow areas such as the Antarctic ice sheet and the accumulation area on the Greenland ice sheet is essentially governed by snow grain size or SSA. Recently, various techniques, including X-ray microtomography (Coléou and others, 2001; Schneebeli and Sokratov, 2004), a gas adsorption method based on Brunauer–Emmett–Teller (BET) theory (referred to here as the BET method; Dominé and others, 2001; Legagneux and others, 2002; Hachikubo and others, 2014), and several optical methods have been proposed to measure the SSA of snow grains as a metric of the size of an ensemble of irregularly shaped snow grains. X-ray microtomography measures the 3-D structure of snow samples, and the BET method measures the surface areas of snow grains. Therefore, in principle, these techniques are expected to be accurate and have been confirmed to be in good agreement (Kerbrat and others, 2008). However, both methods require measurements conducted in a laboratory, and sampling and transporting snow to the laboratory without deteriorating its physical structure.

Optical methods exploit the dependence of snow reflectance at NIR wavelengths on snow grain size. However, because snow reflectance also depends on snow grain shape (Tanikawa and others, 2006; Picard and others, 2009), measurements of snow grain size or SSA by optical methods may include errors when the target snow grains have shapes that differ from the reference grain shape model employed. IceCube (IC; A2 photonics, France) is a well-established, commercially available optical instrument based on the DUal Frequency Integrating Sphere for Snow SSA measurement (DUFISSS; Gallet and others, 2009) instrument that is widely used for field measurements (Gallet and others, 2011, 2014; Carlsen and others, 2017; Vandecrux and others, 2022). IC employs a spherical grain shape model in its retrieval algorithm for deriving SSA from the reflectance of the target snow at a laser wavelength of 1310 nm (Gallet and others, 2009). Because IC requires snow sampling using a sampling cup for each SSA

measurement and a weight of the instrument is heavy (12 kg), it is impractical for expeditious or multipoint observations such as satellite validations or wide-area surveys. Furthermore, the snow sampling procedure might affect the accuracy of the SSA measurement (Martin and Schneebeli, 2023). InfraSnow is a nondestructive optical instrument designed to measure snow grain size through diffuse reflectance at 950 nm. It utilizes an integrating sphere fitted with a light-emitting diode light source (Gergely and others, 2013). This handheld device provides rapid measurements, typically requiring only several seconds for 10 measurements. It is important to note that InfraSnow necessitates snow density as a secondary input parameter. This is because the instrument's reflectance measurements are influenced not only by snow grain size but also by snow density. The estimated accuracy, when compared to reference snow grain size measurements obtained through micro-computed tomography, is 25%, accounting for uncertainties in snow density. Here, we report the development of a Handheld Integrating Sphere Snow Grain Sizer (HISSGraS) for field use. We observed SSAs using the HISSGraS, IC, and BET methods in a snowfield in eastern Hokkaido, Japan. Then, we conducted an intercomparison of the three techniques based on the obtained SSA data. We used the SSAs measured with the BET method as reference values because, among these three techniques, the BET method is, in principle, the most direct for measuring SSA. The accuracy of BET measurements has been estimated to be 12% (Legagneux and others, 2002). Additionally, the BET method is applicable over a wide range of SSAs, and Legagneux and others (2002) reported SSAs for samples exceeding 150 m^2 kg^{-1}. Thus, SSA measurements with HISSGraS were obtained using two different in situ measurement methods (snow sample and direct measurement) and applying two different snow grain shape models to the SSA retrieval algorithm (spherical and nonspherical). We compared these four types of SSAs derived from HISSGraS with SSAs derived from the IC and BET methods to assess the accuracy of the HISSGraS instrument.

2. Instrumentation

2.1. The HISSGraS instrument

HISSGraS was designed to measure the SSA of snow grains on site (Fig. 1). The characteristics of HISSGraS are: (1) lightweight (1.7 kg, including the battery), (2) handheld size (L 287 mm long × 109 mm high × 104 mm wide), (3) measuring the snow surface or a snow pit face directly through a glass window installed in front of an integrating sphere (IS) (Fig. 1, top right) and (4) recording the measured data and GPS measurement position automatically on a memory card. The measurement duration for a single data point is less than 1 s. These enable HISSGraS quick field measurements. HISSGraS can also measure SSA of snow samples collected using the same sampling cup and procedure as the IC. A cylindrical snow core, 30 mm thick, is extracted using a snow sampler and then inserted into a sampling cup with a depth of 25 mm using a piston. Any excess snow is carefully removed with a snow spatula to provide a fresh surface. The use of a sampling cup during the sampling procedure could introduce errors in SSA measurements. Martin and Schneebeli (2023) discussed how particles artificially created during the sampling procedure using a sampling cup in SSA measurements with the IC method sometimes led to overestimated SSAs when compared to SSAs derived from X-ray microtomography. Additionally, Gallet and others (2009) pointed out that snow samples with low density and high SSA (>66 m^2 kg^{-1}) could produce artifacts, where incident light hits the walls or bottom of the sampling cup, causing underestimated SSAs. Therefore, performing

SSA measurements directly on a snow surface or a snow pit face using HISSGraS (as described in (3)) is expected to minimize errors related to these technical issues.

When measuring directly at the snow surface or a snow pit wall, the snow window of HISSGraS is gently pressed against the target snow surface or snow pit face, creating a contact of approximately 5 to 10 mm in depth, ensuring that the snow microstructure is not significantly disturbed. To prevent stray light from entering during snow pit measurements, a black cloth was placed over the snow surface (Fig. 1). For all HISSGraS measurements directly at the snow surface, a sheltering disk (bottom right of Fig. 1) was utilized to prevent stray light interference. After conducting tests to assess the impact of stray light under direct solar illumination without the sheltering disk, we observed no significant differences in the HISSGraS output. As a result, we chose not to use a sheltering disk when measuring directly at the snow pit wall (main picture in Fig. 1). It is worth noting that achieving a perfect seal of the snow window against the snow pit face can be challenging in case the snow layers containing ice formations or large, hard ice grains.

The basic measurement principle of the HISSGraS instrument is the same as that of the IC instrument (Gallet and others, 2009). HISSGraS uses an IS to measure the reflectance of the target snow R_s at the wavelength of the laser diode used as the light source (λ_L = 1310 nm). The interior wall of the IS is painted with BaSO$_4$, and the laser diode illuminates the target snow through a snow window (Fig. 1). To obtain the reflectance of the target snow, the light intensity on the IS wall is measured with an InGaAs photodiode detector. Then, the measured light intensity is converted to R_s using calibration data obtained for six different Spectralon diffuse reflectance standards (DRSs). Because the beam intensity output from a laser diode generally has temperature dependence, HISSGraS records the temperature of the laser diode (T_L) together with the output signal from the detector to correct the T_L dependence of the laser power. Figure 2a shows the T_L dependence of the HISSGraS output signals for the six Spectralon DRSs (#1–#6) obtained during field observations (see Section 3) and used for calibration data. The temperature dependence of the HISSGraS output, as illustrated in Figure 2a, is approximately 1.2% K^{-1} within the temperature range of −2 to 12°C. In contrast, the InGaAs photodiode used in this study exhibits a temperature dependence of approximately ± 0.1% K^{-1} at 25°C. Therefore, it is reasonable to attribute the temperature dependence observed in Figure 2a to the laser's temperature sensitivity. Ideally, this calibration procedure should be performed before and after each set of SSA measurements (we did so in this study), because air temperature variations, for example, during the observation might influence SSA profile measurements conducted in a snow pit, but the relationship between T_L and the HISSGraS output signal can also be determined by using calibration data obtained in a cold laboratory. The dashed curves in Figure 2a are fitted using a cubic polynomial function at six reflectance values of Spectralon DRSs, from which the relationships between the output signal and six reflectance values shown by closed circles in Figure 2b are obtained. Although we show the HISSGraS output signal–T_L-corrected reflectance R_S relationships for T_L at 5°C intervals (Fig. 2b), the relationship can be determined for any T_L from the temperature-dependence curves shown in Figure 2a. From those closed circles, the solid curves shown in Figure 2b are furthermore fitted with a cubic polynomial function, which are the relational equations to obtain the T_L-corrected reflectance R_s from the HISSGraS output signal. HISSGraS only emits a laser beam during SSA measurements due to battery consumption and safety reasons, whereas IC always emits a laser beam continuously. It is recommended for IC to warm up with laser emission sufficiently before taking SSA measurements. We

Figure 1. Direct measurement of a snow pit face with the HISSGraS instrument. A black cloth covers the snow surface to protect against stray light from solar radiation entering the HISSGraS instrument. The inset photo at top right shows the front of the HISSGraS and the glass window (snow window) installed in the open port of the IS. The diameter of the window aperture is 25 mm. The inset photo at bottom right shows HISSGraS with a sheltering disk attached to prevent stray light from penetrating through the snow surface during the snow surface measurements. The diameter of the sheltering disk is 150 mm.

allowed the HISSGraS device itself to warm up for 30 min before conducting measurements in this study, while the laser only emits during the actual measurement process. As demonstrated in Figure 2a, which was generated from all calibration data collected over the entire observation period, a consistent relationship between laser power and temperature is evident. Therefore, errors stemming from the lack of laser warm-up are expected to be minimal. HISSGraS is conceptually similar to InfraSnow; however, it employs different wavelengths. Given that the light penetration depth at 1310 nm for HISSGraS is shallower than that at 950 nm for InfraSnow, HISSGraS provides SSA information for a shallower snow layer (approximately several millimeters) compared to InfraSnow (approximately several centimeters). Since InfraSnow does not have a glass window in front of the integrating sphere, it is expected to nondestructively measure the SSA of the snow surface or snow pit face, including wet snow.

2.2. SSA retrieval algorithm

2.2.1. Structure of the IS and illumination properties of the target snow

Figure 3 illustrates the structure of the IS and the illumination properties of the snow by the light emitted from the laser diode in the IS. The direct laser beam as a light source initially illuminates the target snow surface through the glass snow window in front of the HISSGraS instrument and is reflected diffusely into the IS. After the first reflection, multiple diffuse light reflections occur in the IS; thus, the target snow is illuminated hemispherically with diffuse light (Fig. 3a). These illumination processes occur with a single laser emission. The photodiode detector observes the light intensity on the interior wall of the IS. The first reflectance of the target snow is the nadir directional reflectance ($\dot{r}$) and the second, diffuse reflectance is the hemispherical reflectance (r). The theoretically expected reflectance of the target snow R_s is expressed as:

$$R_s = f_f^{\downarrow} r + (1 - f_f^{\downarrow}) \dot{r}, \qquad (1)$$

where $f_f^{\downarrow}$ is the diffuse fraction of the total illumination of the target snow. The value of $f_f^{\downarrow}$ can be calculated using $\dot{r}$, r, the IS structural parameters given below, the interior wall reflectance of the IS ($\omega = 0.925$) at λ_L, and the laser emission fractions initially striking the target snow ($\dot{f} = 0.885$) and the IS wall ($1 - \dot{f}$) (Hidović-Rowe and others, 2006; Gallet and others, 2009) as:

$$f_f^{\downarrow} = \omega s \frac{\dot{f} \dot{r} \alpha + (1 - \dot{f})\{1 - (s+d)\}}{1 - (s+d) - \omega\alpha[1 - \{d + (1-r)s\}]}. \qquad (2)$$

The structural parameters of the IS are shown in Figure 3b, which are the surface area fractions of the photodiode detector ($d = 0.010102$), target snow window ($s = 0.066987$), laser diode ($h = 0.010102$), and reflective IS wall ($\alpha = 0.91281$), where $d + s + h + \alpha = 1$. The value of ω was measured directly using HISSGraS with a BaSO$_4$ reflectance standard, the same material as the IS wall. The measurement of f was conducted under condition where no external light entered the IS from the snow window.

Eqns (1) and (2) relate the reflectance of the target being measured (R_s) to the signal detected by the photodiode. To obtain SSA from R_s, the two types of reflectances, $\dot{r}$ and r, at λ_L as a function of SSA are calculated with a radiative transfer model (Aoki and others, 1999, 2000), where $\dot{r}$ is calculated for direct beam illumination to the nadir direction from the laser diode, and r is calculated for the diffuse illumination from the IS wall. The relationships between SSA and $\dot{r}$ and between SSA and r are obtained, which will be shown in the following section. Finally, R_s is derived as a function of SSA by using Eqns (1) and (2).

2.2.2. Snow grain shape model

The radiative transfer calculations to establish the R_s–SSA relationships involve three steps. The first step is to calculate the single-scattering parameters of the snow grains, utilizing both spherical and nonspherical snow grain shape models. We calculated the spherical model using Mie theory with a log-normal size distribution (Aoki and others, 1999, 2000) and the
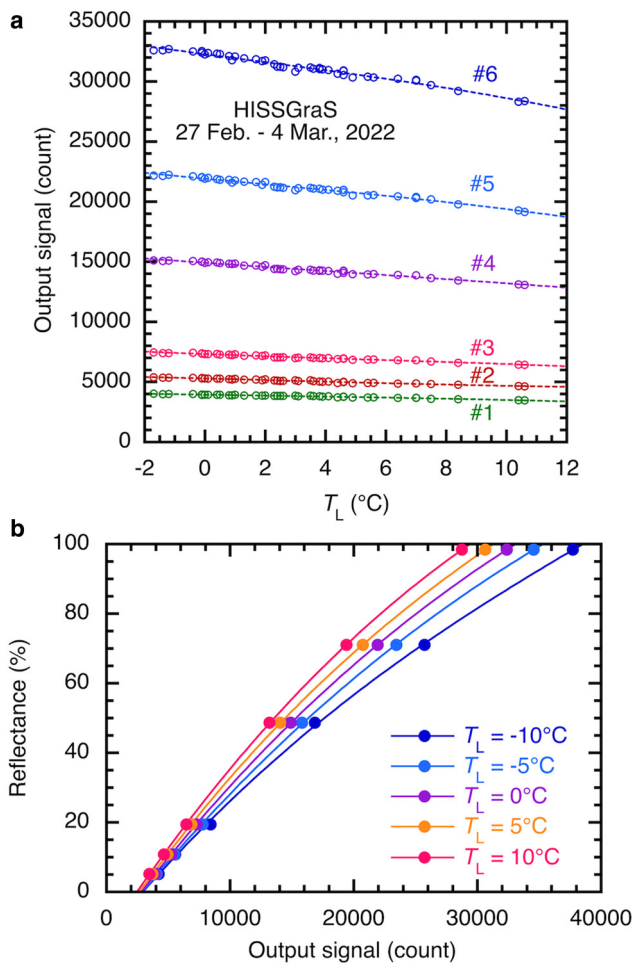
Figure 2. (a) Laser temperature (T_L) dependence of the HISSGraS output signal calibrated by using six Spectralon DRSs (#1–6) obtained during the in situ field observation period from 27 February to 4 March 2022 at Nakasatsunai, Hokkaido, Japan. The reflectances of DRSs #1–6 at laser wavelength $\lambda_L = 1310$ nm are 5.1, 10.7, 19.3, 48.6, 71.0 and 98.3%, respectively. Curves (dashed lines) were fitted to the calibration data (HISSGraS output signal–T_L relationship; open circles) using a cubic polynomial function. (b) Relationships between the HISSGraS output signal and reflectance for different T_L values (5°C intervals). The solid curves were fitted to the data calculated from the fitting curves shown in (a) for DRS reflectances #1–6 (closed circles) using a cubic polynomial function.
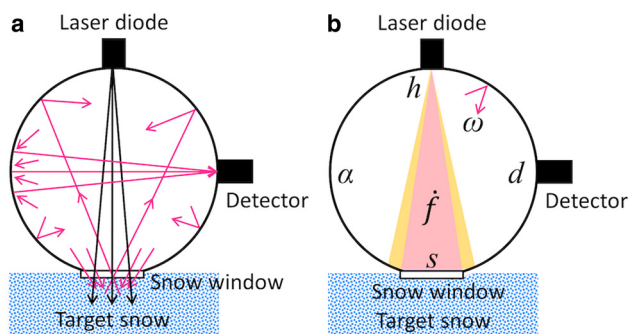
Figure 3. Schematic illustrations of laser light paths in the IS and its components: (a) Pathways of light emitted from the laser diode and the illumination conditions of the target snow. The direct beam emitted from the laser diode is indicated by black arrows, and the reflected light by the target snow and the interior wall of the IS is shown with pink arrows. The laser direct beam illuminates the interior wall of the IS, extending beyond the snow window. The detector measures the intensity of the reflected light on the opposite interior wall of the IS. (b) Structural parameters of the IS components. The surface area fractions of the components are d, photodiode detector; s, snow window; h, laser diode; and α, reflective IS wall. ω represents the reflectivity of the IS wall and $\dot{f}$ is the fraction of light initially striking the target snow (pink-colored area) relative to the total laser emission (orange-colored area).
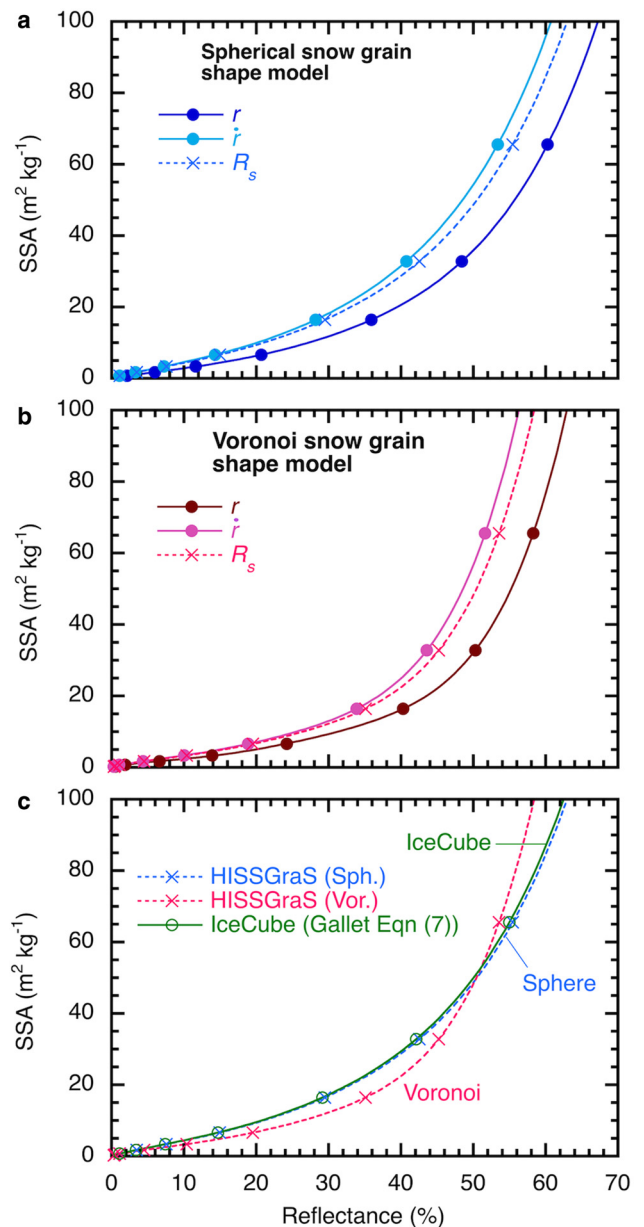
Figure 4. Relationships between snow reflectance at $\lambda_L = 1310$ nm and SSA of snow grains calculated with a radiative transfer model using a (a) spherical or (b) Voronoi (nonspherical) grain shape models. Solid curves in (a) and (b) show the relationships of SSA with nadir directional reflectance ($\dot{r}$) and hemispherical reflectance (r), and the dashed curves show the HISSGraS reflectance (R_s)–SSA relationship calculated with Eqns (1) and (2). (c) The HISSGraS R_s–SSA relationships calculated with the spherical and Voronoi models (HISSGraS (Sph.) and HISSGraS (Vor.), respectively; i.e. the dashed curves from (a) and (b)), and the IceCube R_s–SSA relationship (Gallet and others, 2009). In each panel, quintic polynomial curves were fitted to the values theoretically calculated with the radiative transfer model (symbols) (Aoki and others, 1999, 2000).

nonspherical model using the Voronoi shape model (Ishimoto and others, 2012, 2018). Using X-ray micro-computed tomography data for various types of snow grains, Ishimoto and others (2018) showed that the single-scattering parameters of fine snow particles can be accurately parameterized by a Voronoi column model and those of coarse snow particles by a Voronoi aggregate model. The transition from the Voronoi column shape to the Voronoi aggregate shape occurs at an SSA-equivalent sphere grain radius ($r_{VA} = 3/(\rho_{ice}SSA)$) between $r_{VA} = 50\ \mu m$ and $r_{VA} = 200\ \mu m$, where ρ_{ice} is ice density and the unit of SSA is area per unit weight. The validity of this Voronoi column/aggregate grain shape model for retrieving snow grain size has been

confirmed by observations using a ground-based spectral radiometer in Hokkaido, Japan (Tanikawa and others, 2020). In this study, as the nonspherical grain shape model, we used the same Voronoi column/aggregate model used by Ishimoto and Others (2018) and Tanikawa and Others (2020).

In the second step, we calculated the relationships between snow reflectance $\dot{r}$ and r at λ_L and the SSA of snow using a multiple scattering radiative transfer model (Aoki and others, 1999, 2000). This calculation involved inputting the single-scattering parameters of the snow grains determined in the first step. The relationships between the reflectance and SSA for both spherical and nonspherical (Voronoi) snow grain shape models are shown by solid curves in Figures 4a and b, respectively. These curves were fitted with quintic polynomials to match the discrete values obtained through theoretical calculations using a radiative transfer model. When viewing horizontally at the same SSA value, the curve for r is higher than that for $\dot{r}$. As the third step, for each grain shape model, we calculated the R_s–SSA relationships from $\dot{r}$ and r by Eqn (1) (Figs 4a and b, dashed curves). Then, we compared the R_s–SSA relationships obtained with the spherical and Voronoi models with that for IC (Eqn (7) in Gallet and others, 2009). The R_s–SSA relationship curve for the HISSGraS spherical model mostly overlaps with the IC curve, but we consider this agreement to be merely fortuitous. For $R_s < 50\%$ (SSA $< 52\,\mathrm{m^2\,kg^{-1}}$), the curve obtained with the Voronoi model is lower than those obtained with the spherical model and the IC curve, but the relationship is reversed for $R_s > 50\%$. This reversal occurs because of the change of the Voronoi model from the aggregate to the column shape as SSA increases. We used these relational equations to convert the T_L-corrected HISSGraS-measured reflectance R_s at λ_L to SSA.

3. Field observations

3.1. Observation site

SSA measurements were conducted together with snow pit observations from 27 February to 4 March 2022 in a flat snowfield at Nakasatsunai (42°38.4′N, 143°6.6′E; 251 m a.s.l.) in Hokkaido, Japan (Fig. 5). The fieldwork was conducted during 08:00–12:30 local time (LT) (Fig. 6) to synchronize with satellite overpasses,
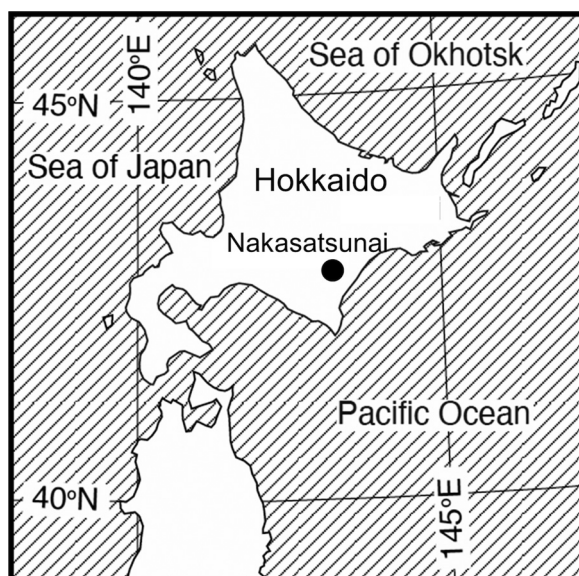

Figure 5. Location of the Nakasastunai observation site (42°38.4′N, 143°6.6′E; 251 m a.s.l.), Hokkaido, Japan. The ground-surface at the 450 m × 520 m observation site was flat farmland.

including the Second Generation Global Imager (SGLI) on the Global Change Observation Mission-Climate (GCOM-C) satellite and the Moderate Resolution Imaging Spectroradiometer (MODIS) on Terra satellite. The snow height during the observation period was 54–65 cm, and the daily maximum air temperature was above 0°C from 27 February to 2 March and just below 0°C on 4 March (Table 1). Because it snowed strongly on 3 March, field observations were not conducted at the Nakasatsunai site on that date, although SSA measurements for the snow surface, consisting of precipitation particles, were performed during 15:00–16:00 LT near the facility at Kamisatsunai, 1.5 km away from the Nakasatsunai site (Fig. 6).

3.2. SSA and snow pit observations

At Nakasatsunai, we performed in situ SSA measurements with the HISSGraS and IC instruments, snow sampling for later laboratory measurement with the BET method, and snow pit observations and other observations for the satellite validation experiment, including spectral albedo, bidirectional reflectance, and infrared radiation. The relative timing of the snow pit observations, SSA measurements, and snow sampling for BET method measurements are shown in Figure 6. SSA profile measurements were first performed with both the IC and HISSGraS instruments on snow samples collected from a snow pit face at 3-cm intervals with the same 25-mm-deep sampling cup used for IC-based measurements ('IC&HIS$_s$' in Fig. 6). Subsequently, SSA profile was measured applying HISSGraS directly on the snow pit wall, though on a new pit face ('HIS$_d$' in Fig. 6). Snow was sampled for the BET measurements ('BET' in Fig. 6) from another, nearby snow pit; thus, the snow samples used for the BET measurement were different from those used for IC and HISSGraS measurements. For the BET measurements, snow samples of 12–25 g were collected in stainless steel pressure cells (internal volume, 42 mL) that were immediately immersed in liquid nitrogen at the field site and transported to a temporary laboratory established at Kamisatsunai. The SSAs of the snow samples were measured on the same day as the samples were collected with a portable BET instrument based on methane adsorption (described in detail in Hachikubo and others, 2014). Between SSA profile measurements, we measured surface snow SSAs in the same area applying both IC and HISSGraS (HIS$_s$) on snow samples (marked, respectively, as IC and HIS$_s$ in Fig. 6) and HISSGraS directly on the surface (HIS$_d$ in Fig. 6). SSA profiles measured with IC and HIS$_s$ on snow samples, with HIS$_d$, and with the BET method on snow samples are plotted in Figure 7. Surface snow SSAs, measured with the same methods used for the SSA profiles, were not synchronous with BET method measurements. After the other SSA measurements on 2 and 4 March, multipoint surface SSA observations were conducted with HIS$_{dmp}$ at 110 and 108 points, respectively, along a route approximately 4.5 km long around the snow pit area in the same farm field. No snow pit observations were performed on 3 March because of strong snowfall, and SSA was measured only on surface snow composed of precipitation particles. On 28 February and 2 March, SSA profile measurements with IC and HIS$_s$ were conducted separately at different times for the upper and lower layers in the snow pit. SSA profile observations with IC or HIS$_s$ took approximately 30 min per 20 snow samples, whereas SSA profile observations with HIS$_d$ on the same snow pit wall took approximately 3 min; thus, HIS$_d$ observations required only ~1/10 of the time required for IC and HIS$_s$.

Snow pit observations were performed approximately 15 m away from the snow pits used for SSA measurements on each day of the observation period except 3 March, when there was strong snowfall (Fig. 6). The snow pit observations included the
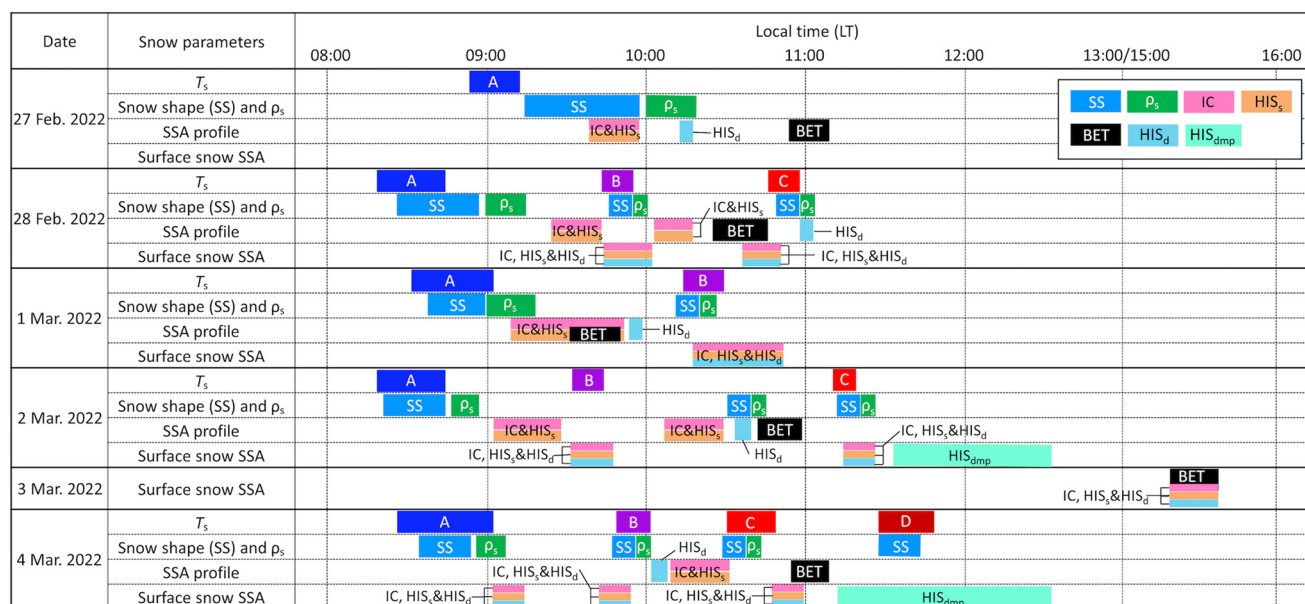
Figure 6. Relative timing of snow pit observations and SSA measurements at Nakasatsunai from 27 February to 4 March 2022. The lengths of the color bars indicate the actual time period in which the corresponding measurements were performed. Snow temperature (T_s) profiles were measured during time periods indicated with color bars A, B, C and D. The occurrences of snow grain shape and snow density are marked with SS and ρ_s, respectively. SSA measurements are indicated by the abbreviation of the corresponding measurement instrument or method: IC, HIS_s and BET represent SSA measurements carried out on snow samples using IceCube, HISSGraS and BET method, respectively, while HIS_d indicates SSA measurements directly performed on the snow pit wall or at the snow surface using HISSGraS. Multipoint direct surface SSA observations conducted with HISSGraS are marked as HIS_{dmp}. The top right inset shows the abbreviations of the snow parameters and SSA measurement methods and their corresponding colors.

vertical profiles of snow temperature (T_s), snow shape (SS), snow density (ρ_s), optically equivalent snow grain size measured with a magnifying glass (as defined by Aoki and others, 2000, 2003), liquid water content, and snow microphotograph. The three components after optically equivalent snow grain size are excluded from Figure 6 because they are not addressed in the paper.

4. Results and discussion

4.1. Snow pit observations

We performed snow pit observations one to four times a day (Fig. 6). Vertical profiles of T_s, ρ_s, and SS are shown in Figure 8, in which SS and ρ_s data from only the first observation on each day shown in Figure 6 are plotted. The air temperature increased to above 0°C every day of the observation period until 2 March (Table 1). T_s near the snow surface also increased to the melting point by around 11:00 LT on those days, but the underlying snow layer remained well below the melting point during the morning. Weak snowfall was observed on 27 February and 1 March and strong snowfall on 3 March. Snow height decreased

during the first four warm days but increased on 4 March due to the snowfall on 3 March. The thickness of the snow layer above the ice formations also decreased during the first four days, suggesting surface snow melting. Snow grain Melt Forms were observed on 27–28 February and 2 March as well as during the second and third snow pit observations after 09:31 LT on 1 March. Precipitation particles were observed in the surface layer on 2 March and 4 March. The snow layers below 45 cm snow height consisted mainly of faceted crystals and melt forms, but the bottom layer contained depth hoar near the ground-surface, where T_s was close to the melting point. Meteorological conditions at Nakasatsunai during the observation period in 2022 were warmer than an average year and thus snow conditions were variable throughout each day.

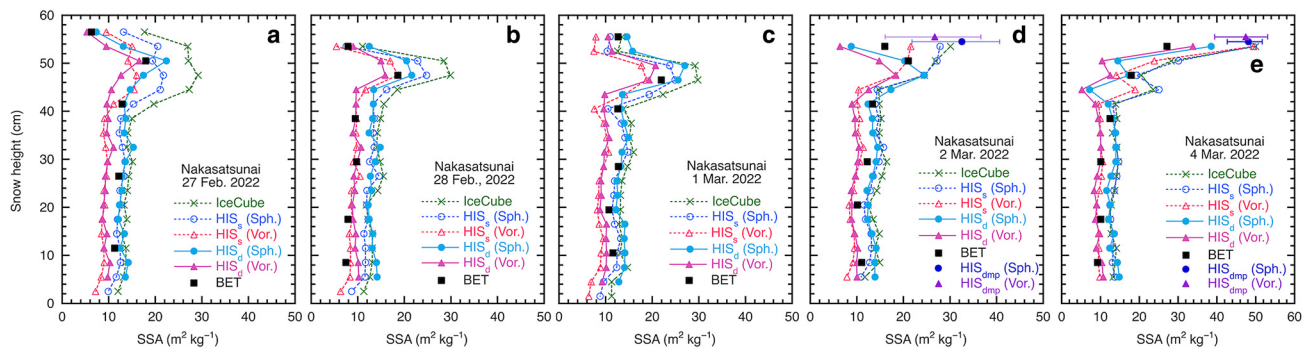### 4.2. Vertical SSA profiles

Vertical SSA profiles during the observation period, except 3 March, measured with the HISSGraS, IC and BET methods are plotted in Figure 7. Four HISSGraS profiles were obtained:

Table 1. Snow and meteorological conditions during the observation period at Nakasatsunai

Date in 2022	27 February	28 February	1 March	2 March	3 March	4 March
Snow height (cm)	65	58	58	54	No data	58
Weather condition	Snowfall	Cloudy	Cloudy	Clear	Snowfall	Clear
Time (LT)			Air temperature (°C)			
08:00	2.1	−0.7	−2.1	−3.2	−6.5	−4.7
09:00	0.5	−0.1	−0.8	−3.4	−5.7	−4.0
10:00	0.5	0.2	1.4	−1.6	−5.5	−1.4
11:00	0.1	0.6	1.3	−1.3	−4.7	−0.8
12:00	0.3	0.6	0.7	−1.1	−3.6	−0.7
13:00	0.2	−0.8	0.9	0.2	−5.1	−0.7
14:00	0.4	−1.7	0.9	0.4	−4.7	−0.3
15:00	0.6	−1.6	1.1	0.8	−4.3	−0.3

Snow height and weather conditions were measured in situ at the first snow pit observation every day, which is marked with 'A' in Figure 6, and air temperatures are instantaneous values observed at the local time given in the table with the Automated Meteorological Data Acquisition System station of the Japan Meteorological Agency at Kamisatsunai, located 1.1 km from Nakasatsunai.

Figure 7. Vertical profiles of SSA measured on the snow pit face with the HISSGraS, IceCube and BET methods during the observation period. Four different HISSGraS SSA profiles are shown, calculated using the spherical snow particle shape model (Sph.) and the Voronoi snow particle shape model (Vor.) from measurements of snow samples (HIS$_s$) collected from a snow pit and direct measurements (HIS$_d$) on the snow pit face. In (d, e), the mean (blue dot, purple triangle), minimum and maximum (bars) surface SSA observation results derived from multipoint HISSGraS direct measurements (HIS$_{dmp}$) on 2 and 4 March are shown just above the values at surface layer of SSA profiles.

snow sample (HIS$_s$) and direct (HIS$_d$) SSA profiles retrieved using either the spherical (Sph.) or Voronoi (Vor.) model. Fewer data were obtained with the BET method than with the HISSGraS and IC methods because SSA measurement with the BET method is time consuming, approximately 50 min per sample, and must be performed in a laboratory. All SSA profiles measured with the three techniques showed low values of $\sim$10 m^2 kg^{-1} in the snow layers below 40 cm snow height and relatively high values in the subsurface ($\sim$50 cm snow height) and surface layers. Through detailed examination of the SSA profiles derived from the three techniques, we can confirm the following results. (1) HIS$_s$ (Sph.)-derived SSA profiles agreed well with IC profiles on all days, except in the surface and subsurface layers (snow height > 40 cm) on the first three days. (2) HIS$_s$ (Vor.) and HIS$_d$ (Vor.) SSA profiles agreed with each other (hereafter, SSA profile group 1), and HIS$_s$ (Sph.)-, HIS$_d$ (Sph.)-, and IC-derived SSA profiles agreed with each other (hereafter, SSA profile group 2), except in layers above $\sim$48 cm snow height on 2 March and above $\sim$40 cm snow height on 4 March. (3) SSA profile group 1 values were lower than SSA profile group 2 values because of the different R_s–SSA relational equations used for the spherical and the Voronoi models for SSA < 50 m^2 kg^{-1} (Fig. 4c). (4) BET-method SSA profile values were between those of SSA profile groups 1 and 2. (5) In the surface layer, on 2 and 4 March BET method- and HIS$_d$-derived SSA$_s$ were lower than IC- and HIS$_s$-derived SSAs (Figs 7d and e).

Concerning result (1) above, HIS$_s$ (Sph.)-derived SSAs were lower than IC-derived SSAs in both the surface and subsurface layers from 27 February to 1 March (Figs 7a–c). This result can be explained as follows. The daily HIS$_s$ (Sph.)-derived SSA profile measurements were conducted after IC measurements from 09:00 to 10:30 (Fig. 6). During these measurements on those days, the air temperatures were above 0°C (Table 1). Because the air temperature was positive, the temperature of the instrument's body was also positive; thus, contact with the instrument could have melted the snow samples. In the case of the IC measurements, the outer part of each snow sample in the sampling cup was in direct contact with the circular bottom edge of the open port of the IS. In the case of the HISSGraS measurements, the entire glass window was in direct contact with the snow sample. At these contact points, the surface of the snow sample could warm or melt, and the warming/melting would have been significant in the HISSGraS case. Isothermal snow metamorphism might also evolve for snow samples of the HIS$_s$ measurement after the IC measurement on those days. These problems should have been particularly noticeable in the case of snow samples with high SSA because the evolution of SSA by isothermal

metamorphism is described by a logarithmic function (Flin and others, 2004; Legagneux and others, 2004); therefore, high SSAs would have decreased due to isothermal metamorphism at a faster rate than low SSAs. Moreover, if the surface of the snow sample melts, SSA decreases remarkably. Thus, either rapid snow metamorphism or snow sample melting due to positive air temperatures would cause HIS$_s$ (Sph.)-derived SSAs to be underestimated. On the other hand, the findings mentioned earlier, (1) and (2), suggest that when the same grain shape model is employed, the SSAs obtained from snow samples closely resemble those acquired through direct measurements.

With regard to the result (5) above, on 2 and 4 March, snow samples for BET measurements were collected 94 and 50 min later, respectively, than those collected for IC and HIS$_s$ measurements (Fig. 6). However, the respective T_s profiles changed remarkably during the SSA measurements (profiles A–C and B–D in Figs 8d and e, respectively). Hence, the SSAs in the surface layer on those two days might have changed between the time of sample collection for the IC and HIS$_s$ measurements and the time of sample collection for BET measurements. In addition, the snow samples for BET measurements were collected from a different snow pit approximately 2 m from the pit where the IC and HIS$_s$ samples were collected. To assess the impact of the specific sampling location on the SSA measurements, we checked the spatial variability of SSA at the Nakasastunai site. After the snow sampling for BET measurements, multipoint surface SSA observations were carried out with HISSGraS direct measurement (HIS$_{dmp}$) at 110 and 108 points around the snow pit area in the same farm field on 2 and 4 March, respectively (Fig. 6). The spatial distributions of SSA measured at the snow surface with HIS$_{dmp}$ on 2 and 4 March are presented in Figure 9. When comparing these two plots, it becomes evident that on 2 March, when the snow surface temperature had reached the melting point, the SSAs were lower and exhibited greater spatial variability. In contrast, on 4 March, when the snow surface temperature was below freezing point, the SSAs were higher and displayed smaller spatial variability. This contrast in snow surface temperature and the difference in surface layer thickness of the precipitation particles (Fig. 8) are likely causes of the differences observed in the SSA distribution in Figure 9. On both days, the IC- and HIS$_s$-derived SSAs were within the ranges of the HIS$_{dmp}$ values. Meanwhile, SSAs obtained with the BET method and HIS$_d$ SSAs from the snow pit were lower than the minimum HIS$_{dmp}$ (Sph.) and HIS$_{dmp}$ (Vor.) multipoint observation values. Thus, the underestimation of SSA for the surface layer of the snow pit derived from the BET and HIS$_d$ methods cannot be explained by spatial variability of SSA around the study site.
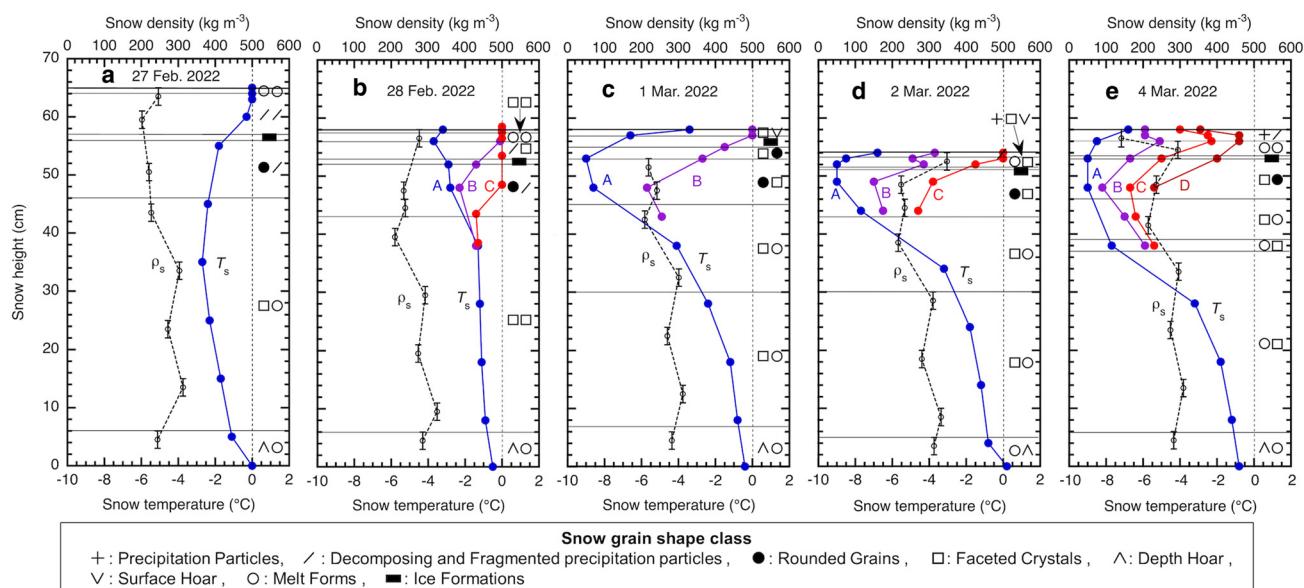
Figure 8. Vertical profiles of snow temperature (T_s), snow density (ρ_s), and snow grain shape observed in a snow pit at Nakasatsunai on (a–e) 27 and 28 February and 1, 2 and 4 March, respectively. Data of SS and ρ_s from only the first observation on each day are plotted (see Fig. 6). In each panel, observed snow grain shapes are shown with the symbols on the right-hand side of the vertical dashed line. The snow grain shape class (bottom) is based on Fierz and others (2009).

We next examined the temporal variations of SSA on 2 and 4 March. T_s in the near-surface layer reached or was close to the melting point (profile C and D in Figs 8d and e, respectively). On those two days, the surface layer also contained precipitation particles, which generally have high SSA; thus, the precipitation particle SSAs could have rapidly decreased by isothermal metamorphism as described above. Hence, a change in the SSA between the time of sample collection for IC and HIS$_s$ measurements and the time of sample collection for BET measurement can explain why SSAs obtained with the BET method were lower than those obtained with the IC and HIS$_s$ measurements in the surface layer on those two days. If the surface snow was melted, the BET snow sampling could cause the underestimation of the BET-method SSAs. This is because putting wet snow with likely some water directly into liquid nitrogen could also alter the SSA by refreezing processes and lowering the SSA due to the bounding of some grains. We measured the liquid water content using a flat dielectric snow wetness device (Denoth and Foglar, 1986) on 2 and 4 March. However, we did not detect any liquid

water on both days. On 2 March, only the snow surface layer (approximately 0–1 cm) reached the melting point, while the snow layer (approximately 1–2 cm) beneath the dielectric sensor remained below the melting point. On 4 March, the snow surface temperature did not reach the melting point during the snow wetness measurement. The underestimation of HIS$_d$-derived SSAs on 2 March also can be explained by the rapid evolution of isothermal metamorphism. However, the HIS$_d$ measurements on 4 March were conducted in the snow pit before the samples for IC and HIS$_s$ measurements were collected; thus, the reason for the underestimation of HIS$_d$-derived SSA in layers above 50 cm snow height and at 44.5 cm snow height on 4 March is unclear. Possible causes are underestimation of the HISSGraS reflectance due to ice formations, as observed in near-surface layers (Figs 8d and e), or a technical issue such as poor contact between the HISSGraS and the target snow pit face. In the case of high SSA and low-density snow (above 50 cm snow height on 4 March), pressing the HISSGraS snow window against the snow surface might disturb the snow microstructure.
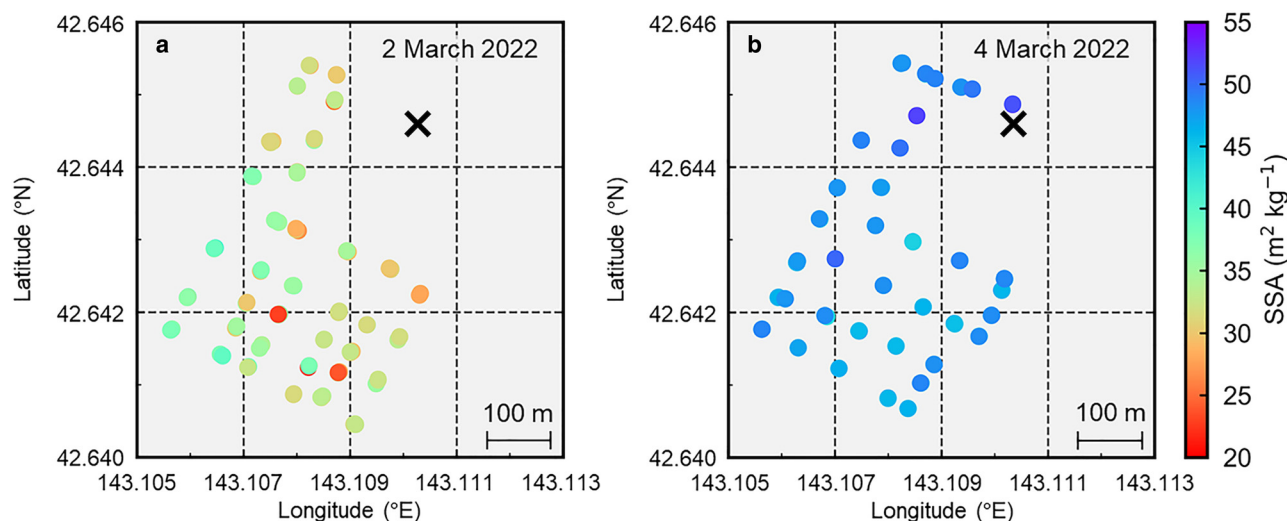
Figure 9. Spatial distribution of SSA of snow surface obtained from multipoint HISSGraS direct measurements (HIS$_{dmp}$) on (a) 2 March 2022 and (b) 4 March 2022. The SSAs are calculated using the spherical snow particle shape model. An 'X' indicates Nakatsunai site.
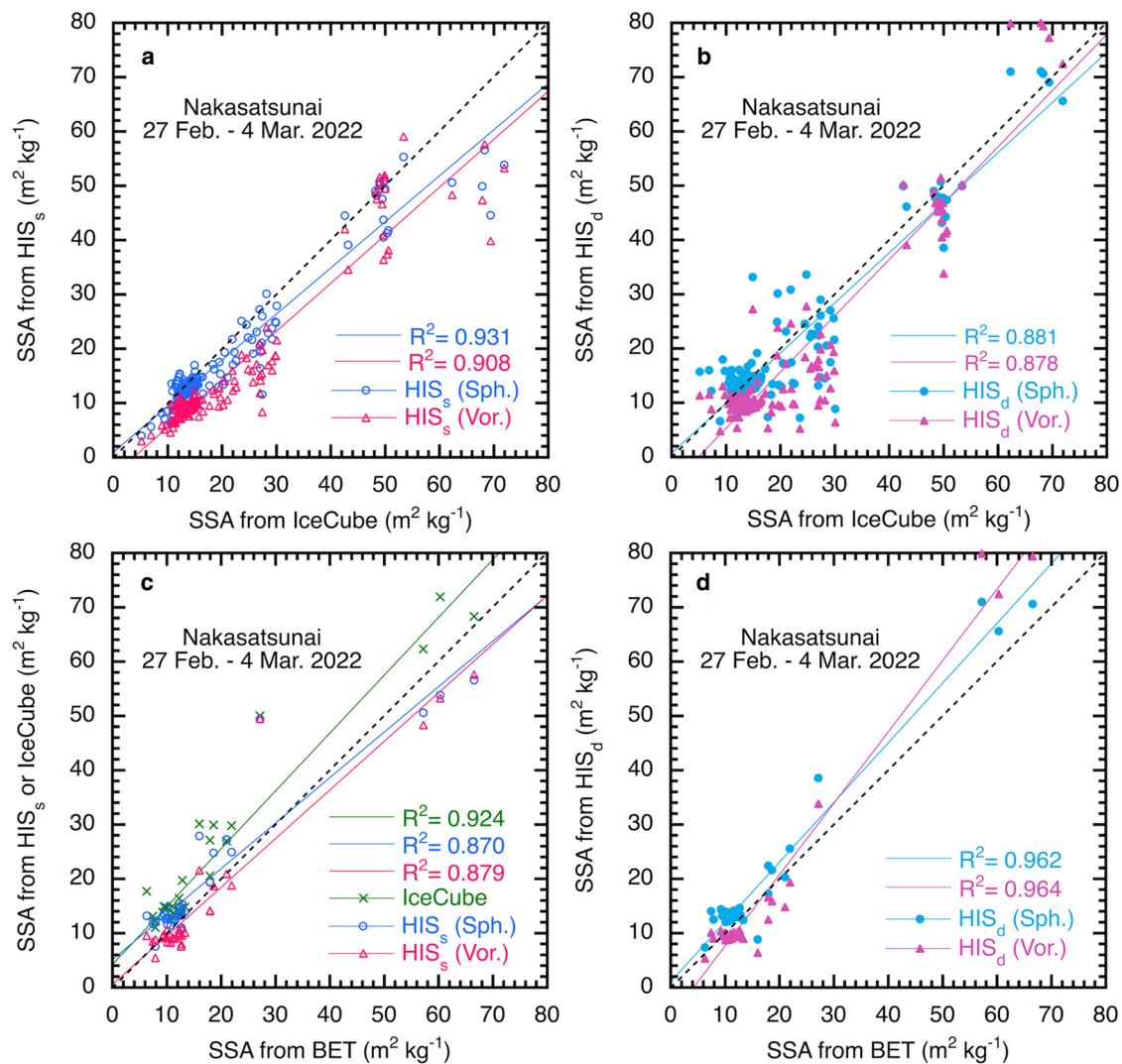
Figure 10. Scatter plots of SSAs derived from the HISSGraS, IceCube and BET methods. (a) IceCube vs HISSGraS SSAs from snow samples collected from the snow pit face and snow surface (HIS$_s$), (b) IceCube vs HISSGraS direct measurements (HIS$_d$), (c) BET vs HISSGraS measured for snow samples (HIS$_s$) and BET vs IceCube and (d) BET vs HISSGraS direct measurements (HIS$_d$). The solid line represents the linear regression line and the dashed line the 1:1 relationship. R^2 is the coefficient of determination associated with the linear regressions.

4.3. Intercomparison of SSAs

We used scatter plots to compare SSAs measured with the HISSGraS, IC and BET methods (Fig. 10) and calculated the mean error, root mean square error (RMSE) and coefficient of determination (R^2) (Table 2). The 10 SSA data points (i.e. five SSA measurement pairs) that showed IC-derived SSAs >60 m^2 kg^{-1} (Figs 10a and b) were observed in the surface layer on 3 March, when the surface snow was composed of precipitation particles.

4.3.1. IceCube vs HISSGraS

Comparisons between the IC-derived SSAs and the HISSGraS-derived SSAs applying HIS$_s$ and HIS$_d$ methods (Fig. 7) are shown in Figures 10a and b, respectively. All SSA observations marked in Figure 6 are included in the comparison except the multipoint SSA measurements HIS$_{dmp}$. The IC-derived SSAs correlated well with HIS$_s$ (Sph.)-derived SSAs ($R^2 = 0.931$, Fig. 10a). This is because the same snow samples were used for both measurements and because the spherical snow grain shape model was used for both SSA retrievals. However, HIS$_s$ (Sph.)-derived SSAs were higher than HIS$_s$ (Vor.)-derived SSAs at the same IC-derived SSAs. This result can be explained by the different R_s–SSA relational equations used for the two snow

grain shape models (Fig. 4). When IC-derived SSAs were higher than 60 m^2 kg^{-1} (Fig. 10a), i.e. in the surface layer when the surface snow was composed of precipitation particles on 3 March, the HIS$_s$ SSAs were lower than the IC-derived SSAs. Hachikubo and others (2014) reported a case in which the SSA of precipitation particles decreased by approximately 10 m^2 kg^{-1} within a few hours after snowfall, even at the low temperature of −19°C, because of the faster isothermal metamorphism of high-SSA snow compared to low-SSA snow (Flin and others, 2004; Legagneux and others, 2004) (see Section 4.2). Thus, the underestimation of HIS$_s$-derived SSA can be attributed to snow metamorphism of the samples occurring after the IC measurements and before the HIS$_s$ measurements.

The IC vs HIS$_d$-derived SSAs (Fig. 10b) showed greater scatter than the IC vs HIS$_s$-derived SSAs (Fig. 10a). Therefore, the R^2 values for IC vs HIS$_d$-derived SSAs (Fig. 10b) are somewhat lower than those for IC- vs HIS$_s$-derived SSAs (Fig. 10a). This is likely because the HIS$_d$ measurements were conducted at different times in the same snow pit, whereas the IC- and HIS$_s$-derived SSAs were obtained from the exact same snow sample. Furthermore, there is a possibility of disturbing the snow microstructure when applying these three optical measurements to snow with high SSA and low density. In the case of the

Table 2. Intercomparison statistics for SSAs ($m^2\,kg^{-1}$) measured with HISSGraS, IceCube (IC), and BET for (a) all snow layers measured, (b) same as the lower five rows in (a) but after the SSAs of the surface layer on 2 and 4 March were excluded, (c) surface and subsurface layers with snow heights exceeding 43 cm on 27–28 February, 54 cm on 1 March, 46 cm on 2 March, 52 cm on 3 March and 43 cm on 4 March and (d) lower layers beneath the layers of (c)

Measurement techniques	Snow grain shape model for HISSGraS	N	MB (m^2 kg^{-1})	RMSE/ mean (%)	R^2
(a)					
IC – HIS$_s$	Sph.	157	2.28	21.6	0.931
IC – HIS$_s$	Vor.	157	5.76	34.4	0.908
IC – HIS$_d$	Sph.	158	0.96	23.9	0.881
IC – HIS$_d$	Vor.	158	4.37	33.5	0.878
BET – HIS$_s$	Sph.	32	−2.26	33.4	0.870
BET – HIS$_s$	Vor.	32	1.32	30.6	0.879
BET – HIS$_d$	Sph.	32	−2.76	25.8	0.962
BET – HIS$_d$	Vor.	32	−0.06	34.3	0.964
BET – IC	–	32	−5.35	40.5	0.924
(b)					
BET – HIS$_s$	Sph.	30	−1.27	22.6	0.968
BET – HIS$_s$	Vor.	30	2.34	20.8	0.984
BET – HIS$_d$	Sph.	30	−2.80	23.0	0.978
BET – HIS$_d$	Vor.	30	−0.03	33.8	0.971
BET – IC	–	30	−4.47	31.5	0.966
(c)					
BET – HIS$_s$	Sph.	12	−2.58	32.4	0.830
BET – HIS$_s$	Vor.	12	0.74	29.9	0.839
BET – HIS$_d$	Sph.	12	−3.40	22.8	0.961
BET – HIS$_d$	Vor.	12	−2.23	34.0	0.968
BET – IC	–	12	−8.30	37.6	0.913
(d)					
BET – HIS$_s$	Sph.	20	−2.06	22.9	0.703
BET – HIS$_s$	Vor.	20	1.67	19.9	0.711
BET – HIS$_d$	Sph.	20	−2.37	26.1	0.623
BET – HIS$_d$	Vor.	20	1.44	19.7	0.633
BET – IC	–	20	−3.58	35.0	0.761

SSAs measured with HISSGraS were obtained both from snow samples (HIS$_s$) and direct measurements (HIS$_d$). Spherical (Sph.) and Voronoi (Vor.) snow grain shape models were employed for the HISSGraS SSA retrievals. N, number of data; MB, mean bias; RMSE/mean, root mean square error normalized by mean SSA, where mean SSA is derived from the first method indicated in the measurement techniques in the table; and R^2, coefficient of determination.

IC-derived SSAs higher than $60\,m^2\,kg^{-1}$, the HIS$_d$ SSAs were comparable to or somewhat higher than the IC-derived SSAs, different from the HIS$_s$-derived SSAs (Fig. 10a). These SSAs were measured from the surface snow, which consisted of precipitation particles with low density on 3 March. Such a fragile snow microstructure can be easily disturbed by the HIS$_d$ measurement when applied directly to the snow surface, as well as by the IC and HIS$_s$ measurements, which require a snow sampling procedure. In general, the snow density of precipitation particles can be variable in the uppermost layer, making it challenging to collect undisturbed samples for IC and HIS$_s$ measurements. Moreover, in the case of low-density snow samples with high SSA ($>66\,m^2\,kg^{-1}$), there is a possibility of artifacts where incident light within the snow sample may strike the walls or bottom of the sampling cup (Gallet and others, 2009). Consequently, SSA measurements using optical techniques for snow grains with high SSA and low snow density near the surface involve technical difficulty. Meanwhile, the values of RMSE/mean between IC- and HIS$_s$-derived SSAs are comparable to those between IC- and HIS$_d$-derived SSAs (Table 2a), suggesting that similar uncertainties are expected between HIS$_s$- and HIS$_d$-derived SSAs.

4.3.2. BET vs IceCube and HISSGraS
We compared all snow pit SSAs (Fig. 7) including the snow surface SSAs on 3 March, between the BET method and IC and between the BET method and HISSGraS (Figs 10c and d, respectively). The SSA data points with BET-derived SSAs higher than $50\,m^2\,kg^{-1}$ were observed for the surface layer on 3 March, when the surface snow was composed of precipitation particles.

We note that in these comparisons, the number of data point comparisons N was only 32, compared with $N = 161$ for the comparisons between the IC and HISSGraS measurements (Figs 10a, b and Table 2a). The BET-method and IC-derived SSAs correlate well ($R^2 = 0.924$, Fig. 10c), whereas the R^2 values between BET- and HIS$_s$ (Sph.)-derived SSAs and between BET- and HIS$_s$ (Vor.)-derived SSAs are somewhat lower. The outliers in Figure 10c $\sim$ BET-derived SSA = $27\,m^2\,kg^{-1}$ represent the surface layer of the snow pit face on 4 March (Fig. 7e). The reason for these outliers, as discussed Section 4.2, is the rapid snow metamorphism of the high-SSA snow consisting of precipitation particles between the sample collection for IC and HIS$_s$ measurements and that for BET measurements 50 min later. When we exclude the underestimated SSA data from the surface layer on 2 and 4 March, all correlations between BET- and IC-derived SSAs, between BET- and HIS$_s$ (Sph.)-derived SSAs, and between BET- and HIS$_s$ (Vor.)-derived SSAs are much improved ($R^2 = 0.966$, 0.968 and 0.984, respectively; Table 2b).

Comparison between BET- and HIS$_d$-derived SSAs (Fig. 10d) showed high correlations of both HIS$_d$ (Sph.)- and HIS$_d$ (Vor.)-derived SSAs with BET-derived SSAs ($R^2 = 0.962$ and 0.964, respectively). Among the four SSA comparisons between BET and HISSGraS, the minimum RMSE/mean was obtained between BET- and HIS$_d$ (Sph.)-derived SSAs (Table 2a). In the case of the data points with BET-derived SSAs $> 50\,m^2\,kg^{-1}$, HIS$_d$ (Vor.)-derived SSAs were overestimated. However, if the underestimated SSAs for the surface layer on 2 and 4 March are excluded, then the correlations between BET- and HIS$_d$ (Sph.)-derived SSAs and between BET- and HIS$_d$ (Vor.)-derived SSAs are improved ($R^2 = 0.978$ and 0.971, respectively; Table 2b). In Figures 10c–d, noticeable deviations from the 1:1 line can be observed for SSA $> 20\,m^2\,kg^{-1}$. In Figure 7, the discrepancies in SSAs among HIS$_s$, HIS$_d$, IC and the BET method are more pronounced in snow layers located 10–15 cm from the surface, where SSAs are higher, compared to the lower layers. To quantify this, we included SSA statistics for the surface and subsurface layers as well as the lower layers (Tables 2c and d). The values of RMSE/mean between the BET method and HISSGraS, as well as between the BET method and IC for the surface and subsurface layers (Table 2c), are generally not better than those for the lower layers (Table 2d). Several factors can contribute to this result, affecting SSA accuracy in the near-surface layer, as previously discussed: (1) rapid snow metamorphism and melting under warm air and high SSA snow conditions, (2) heterogeneities in SSA and snow density near the surface, (3) errors associated with the snow sampling procedure in IC and HIS$_s$ measurements and (4) errors due to the disturbance of snow microstructure caused by a snow window in HIS$_d$ measurements. These issues are more likely to become evident in optical measurements when the air temperature is high.

Using the BET-derived SSAs as references, assuming they are the most accurate, the RMSE/mean values represent the accuracy of the instruments based on this field observation. While optical techniques for measuring snow SSA involve technical difficulties as described above, the RMSE/mean values in Table 2b, excluding two underestimated SSA data points measured with HIS$_d$ and BET methods for precipitation particles under warm conditions, and those in Table 2d for the lower snow layers are generally comparable, except for the BET – HIS$_d$ (Vor.) comparison. Considering these RMSE/mean scores in Table 2b as indicative of the overall accuracy of HISSGraS, it is approximately 21–22% for the HIS$_s$ method and 23–34% for the HIS$_d$ method.

5. Summary

To measure the SSA of snow in the field, we developed a light weight and portable HISSGraS instrument with automatic data

recording. The HISSGraS instrument can be used either for direct measurements of snow surfaces and snow pit faces or for measurements of snow samples collected with a sampling cup. The basic measurement principle is the same as that in the IC method. Because the laser diode used in the HISSGraS instrument as a light source can cause a measurement error, the reflectance should be corrected by monitoring the laser temperature in situ at the time of each measurement. Furthermore, both spherical and nonspherical snow grain shape models are used in the radiative transfer model calculation to convert reflectance values to SSA. The Voronoi snow grain shape model, used as the nonspherical model, changes from a column shape to an aggregate shape depending on the grain size. Thus, four HISSGraS-derived SSAs were obtained by using two in situ measurement methods (snow sample measurement and direct measurement) with either the spherical or Voronoi snow grain shape models used in the SSA retrieval algorithms.

We used the HISSGraS, IC and BET methods to observe SSAs in a snowfield in Hokkaido, Japan, and compared the results among the methods, using the BET method-derived SSA as reference values because they are, in principle, the most accurate. We found that the SSA profiles measured with the IC, BET and four HISSGraS methods were similar during the observation period except for some surface and subsurface layer values. The different results among the three techniques can be attributed to rapid snow metamorphism or snow sample melting under positive air temperatures. When the same grain shape model (spherical or Voronoi model) was used, SSAs from snow samples were similar to those obtained from direct measurements. That is, SSA profiles obtained with the HIS_s (Sph.), HIS_d (Sph.) and IC were similar to each other, and those obtained with the HIS_s (Vor.) and HIS_d (Vor.) were similar to each other. The former three SSA profiles; HIS_s (Sph.), HIS_d (Sph.) and IC were lower than the latter two profiles; HIS_s (Vor.) and HIS_d (Vor.). This is because different R_s–SSA relational equations were used between the spherical model and the Voronoi model. The SSA profiles measured with the BET method generally plot between the former SSA profiles and the latter SSA profiles, except in the surface layer SSAs for 2 and 4 March. Precipitation particles included in the surface snow on those days might have undergone rapid snow metamorphism, or warm conditions may have led to surface snow melting during the SSA measurement period. We also found that the SSA profile observation time using HISSGraS was only about 1/10 as long as that required to measure snow samples collected in a sampling cup.

The IC- and HISSGraS-derived SSAs for snow samples correlated well because the same snow samples were used for both measurements and the spherical snow grain shape model was used for both retrievals. This result suggests that HISSGraS and IC should have similar accuracy as long as the same snow samples and the same snow grain shape model are used. The correlations of SSAs between IC (for snow samples) and HISSGraS direct measurements are somewhat lower than those between IC and HISSGraS for snow samples. This difference may be attributed to the fact that the HISSGraS direct measurements were conducted at different times in the same snow pit as the IC measurements. Furthermore, this discrepancy may be attributed to the disturbance of the snow microstructure during both the snow sampling procedure and direct HISSGraS measurements, which is particularly notable in the near-surface layers with high SSA and low snow density.

BET- and IC-derived SSAs correlate well, whereas BET- and HISSGraS-derived SSAs for snow samples correlate somewhat less well. BET-derived SSAs and SSAs derived from HISSGraS direct measurement correlate better than BET- and HISSGraS-derived SSAs for snow samples. However, the SSAs measured in the surface and subsurface layers with the three techniques show some biases of underestimation. One of the causes would be rapid snow metamorphism of high-SSA precipitation particles or snow melting during the measurement period under warm meteorological conditions. When those underestimated SSA data from the surface layer on 2 and 4 March are excluded, IC- and HISSGraS-derived SSAs from snow samples and SSAs from HISSGraS direct measurement correlate strongly with BET-derived SSAs ($R^2 > 0.96$). Assessing the uncertainty of SSA derived from IC and HISSGraS as references for BET SSA, we observed that the uncertainty is higher for the surface and subsurface layers compared to the lower layers. Several factors may contribute to the uncertainty in SSA for near-surface layers, including rapid changes in snow microstructure under warm conditions, heterogeneities in snow near the surface, and disturbances of snow microstructure due to both snow sampling and direct measurement. Determining the most accurate HISSGraS measurement technique among the four methods used in this study is challenging. Nevertheless, we estimate the overall accuracy of HISSGraS to be approximately 21–22% when employing snow sampling and 23–34% with direct measurement. The choice between a spherical model or a Voronoi model should depend on the snow shape being measured. In the future, conducting comparative experiments involving HISSGraS and IceCube against the BET method or X-ray microtomography should be undertaken, considering various snow shapes under controlled low-temperature laboratory conditions.

Author's contributions. The manuscript was mainly written by T. A. The other authors contributed to the discussion and helped to draft the final version of the manuscript. T. A., T. T., R. I., S. Y., S. M. and J. G. contributed to the development and improvement of the HISSGraS instrument. T. A., Mo. N., M. H. and Ma. N. performed the HISSGraS and IC measurements, and H. A. performed the BET method SSA measurements. A. H., K. S. and S. M. carried out the snow pit observations and Mo. N., Ma. N., T. T., M. S. and R. S. obtained the supporting data during the field observations. T. A., H. I., and T. T. contributed to the radiative transfer calculation and snow grain shape modeling.

References

Aoki T, Aoki T, Fukabori M and Uchiyama A (1999) Numerical simulation of the atmospheric effects on snow albedo with a multiple scattering radiative transfer model for the atmosphere-snow system. *Journal of the Meteorological Society of Japan* **77**, 595–614. doi: 10.2151/jmsj1965.77.2_595

Aoki T and 5 others (2000) Effects of snow physical parameters on spectral albedo and bidirectional reflectance of snow surface. *Journal of Geophysical Research* **105D**, 10219–10236. doi: 10.1029/1999JD901122

Aoki T, Hachikubo A and Hori M (2003) Effects of snow physical parameters on broadband albedos. *Journal of Geophysical Research* **108**, 4616. doi: 10.1029/2003JD003506

Aoki T and 5 others (2011) Physically based snow albedo model for calculating broadband albedos and the solar heating profile in snowpack for general

circulation models. *Journal of Geophysical Research* **116**, D11114. doi: 10.1029/2010JD015507

Carlsen T and 9 others (2017) Comparison of different methods to retrieve optical-equivalent snow grain size in central Antarctica. *The Cryosphere* **11**, 2727–2741. doi: 10.5194/tc-11-2727-2017

Coléou, C and 4 others (2001) Three-dimensional snow images by X-ray microtomography. *Annals of Glaciology* **32**, 75–81. doi: 10.3189/172756401781819418

Denoth A and Foglar A (1986) Recent developments of snow moisture dielectric devices. *International Snow Science Workshop*, Lake Tahoe, California, October, 22–25, 1986, pp. 72–76.

Dominé F, Cabanes A, Taillandier AS and Legagneux L (2001) Specific surface area of snow samples determined by CH4 adsorption at 77 K and estimated by optical microscopy and scanning electron microscopy. *Environmental Science & Technology* **35**(4), 771–780. doi: 10.1021/es001168n

Dominé F, Taillandier AS and Simpson WR (2007) A parameterization of the specific surface area of seasonal snow for field use and for models of snowpack evolution. *Journal of Geophysical Research* **112**, 1–13. doi: 10.1029/2006JF000512

Fierz C and 8 others (2009) The international classification for seasonal snow on the ground. *IHP-VII Technical Documents in Hydrology N°83*, IACS Contribution N°1, UNESCO-IHP, Paris.

Flin F and 4 others (2004) Three-dimensional geometric measurements of snow microstructural evolution under isothermal conditions. *Annals of Glaciology* **38**, 39–44. doi: 10.3189/172756404781814942

Gallet JC, Dominé F, Zender CS and Picard G (2009) Measurement of the specific surface area of snow using infrared reflectance in an integrating sphere at 1310 and 1550 nm. *The Cryosphere* **3**, 167–182. doi: 10.5194/tc-3-167-2009

Gallet JC and 4 others (2011) Vertical profile of the specific surface area and density of the snow at Dome C and on a transect to Dumont D'Urville, Antarctica – albedo calculations and comparison to remote sensing products. *The Cryosphere* **5**, 631–649. doi: 10.5194/tc-5-631-2011

Gallet JC, Dominé F and Dumont M (2014) Measuring the specific surface area of wet snow using 1310 nm reflectance. *The Cryosphere* **8**, 1139–1148. doi: 10.5194/tc-8-1139-2014

Gergely M, Wolfsperger F and Schneebeli M (2013) Simulation and validation of the InfraSnow: an instrument to measure snow optically equivalent grain size. *IEEE Transactions on Geoscience and Remote Sensing* **52**, 4236–4247. doi: 10.1109/tgrs.2013.2280502

Hachikubo A and 9 others (2014) Effects of temperature and grain type on time variation of snow specific surface area. *Bulletin of Glaciological Research* **32**, 47–53. doi: 10.5331/bgr.32.47

Hidović-Rowe D, Rowe JE and Lualdi M (2006) Markov models of integrating spheres for hyperspectral imaging. *Applied Optics* **45**, 5248–5257. doi: 10.1364/AO.45.005248

Ishimoto H and 4 others (2012) Irregularly shaped ice aggregates in optical modeling of convectively generated ice clouds. *Journal of Quantitative Spectroscopy and Radiative Transfer* **113**, 632 643. doi: 10.1016/j.jqsrt.2012.01.017

Ishimoto H and 5 others (2018) Snow particles extracted from X-ray computed microtomography imagery and their single-scattering properties. *Journal of Quantitative Spectroscopy and Radiative Transfer* **209**, 113–128. doi: 10.1016/j.jqsrt.2018.01.021

Kerbrat M and 5 others (2008) Measuring the specific surface area of snow with X-ray tomography and gas adsorption: comparison and implications for surface smoothness. *Atmospheric Chemistry and Physics* **8**, 1261–1275. doi: 10.5194/acp-8-1261-2008, 2008

Legagneux L, Cabanes A and Dominé F (2002) Measurement of the specific surface area of 176 snow samples using methane adsorption at 77 K. *Journal of Geophysical Research* **107**(D17), 4335. doi: 10.1029/2001JD001016

Legagneux L, Taillandier AS and Domine F (2004) Grain growth theories and the isothermal evolution of the specific surface area of snow. *Journal of Applied Physics* **95**, 6175–6184. doi: 10.1063/1.1710718

Martin J and Schneebeli M (2023) Impact of the sampling procedure on the specific surface area of snow measurements with the IceCube. *The Cryosphere* **17**, 1723–1734. doi: 10.5194/tc-17-1723-2023

Picard G, Arnaud L, Dominé F and Fily M (2009) Determining snow specific surface area from near-infrared reflectance measurements: numerical study of the influence of grain shape. *Cold Regions Science and Technology* **56**, 10–17. doi: 10.1016/j.coldregions.2008.10.001

Schneebeli M and Sokratov SA (2004) Tomography of temperature gradient metamorphism of snow and associated changes in heat conductivity. *Hydrological Processes* **18**, 3655–3665. doi: 10.1002/hyp.5800

Tanikawa T and 5 others (2006) Monte Carlo simulations of spectral albedo for artificial snowpacks composed of spherical and non-spherical particles. *Applied Optics* **45**, 5310–5319. doi: 10.1364/AO.45.005310

Tanikawa T and 10 others (2020) Effects of snow grain shape and mixing state of snow impurity on retrieval of snow physical parameters from ground-based optical instrument. *Journal of Geophysical Research: Atmospheres* **125**, e2019JD031858. doi: 10.1029/2019JD031858

Vandecrux B and 8 others (2022) The determination of the snow optical grain diameter and snowmelt area on the Greenland ice sheet using spaceborne optical observations. *Remote Sensing* **14**, 932. doi: 10.3390/rs14040932

Warren SG and Wiscombe WJ (1980) A model for the spectral albedo of snow. II: snow containing atmospheric aerosols. *Journal of the Atmospheric Sciences* **37**, 2734–2745. doi: 10.1175/1520-0469(1980)037<2734:AMFTSA>2.0.CO;2

Wiscombe WJ and Warren SG (1980) A model for the spectral albedo of snow, I: pure snow. *Journal of the Atmospheric Sciences* **37**, 2712–2733. doi: 10.1175/1520-0469(1980)037<2712:AMFTSA>2.0.CO;2